Energy Advances

PAPER

View Article Online
View Journal | View Issue

Check for updates

Cite this: *Energy Adv.*, 2025, 4, 1529

Received 20th June 2025,
Accepted 20th October 2025

DOI: 10.1039/d5ya00164a

rsc.li/energy-advances

# Effect of fluorinated arylammonium halide passivation in chloride–iodide perovskite solar cells

Ashraful Hossain Howlader, *[a] Yin Yao,[b] Rhiannon Kuchel[b] and Ashraf Uddin *[a]

Due to the radius mismatch between iodine and chlorine, ion migration is unavoidable in chloride–iodide perovskites. The presence of atomic vacancies in the solution-processed perovskite thin film works as a route of ion migration. Here, we investigate the consequence of the ion migration in chloride–iodide perovskite solar cells. We use $FA_{0.6}MA_{0.4}PbI_{2.7}Cl_{0.3}$ as the active perovskite layer. We passivate the top surface of the chloride–iodide perovskite thin film with mixed 4-fluorobenzylammonium chloride and 4-fluorobenzylammonium bromide. We observe that fluorinated benzylammonium halides show better passivation and hydrophobicity. Compared to the non-passivated solar cells, we get a significant fill factor and stability improvement. We get 76.44% fill factor from our passivated solar cell. Besides, our passivated solar cell offers a photo conversion efficiency of 21.10%. Moreover, we also get about 80% stability without encapsulation after 56 days.

## 1. Introduction

The efficiency of perovskite solar cells (PSCs) is increasing rapidly, which is a promising sign for developing next-generation solar cells.[1] With a bonus point of a low-temperature solution process facility, it is possible to fabricate PSCs through less expensive roll-to-roll mass production for commercialization.[2] Still, we have to face many challenges to achieve the goal. The pinholes and grains in the bulk of the solution-processed perovskite thin film are a pervasive problem. Non-uniformity with a rough surface is another prevalent problem in the solution-processed perovskite thin film. The interface between the perovskite active and charge transport layers (CTLs) contains many defects. The bulk and interface defects are the sources of defect states and the centers for electron–hole recombination.[3,4] The photogenerated electrons get trapped by these trap states and cannot reach the electrodes. As a result, the photo conversion efficiency (PCE) is significantly reduced.

Very recently, perovskite precursors with long or bulky organic cations and loosely bound halogens have been applied as passivators at the interface of PSCs.[5] This passivation could heal the perovskite layer's surface and bulk defects. The small halogens can readily diffuse into the bulk and fill the atomic vacancy positions. The long or bulky organic cations remain on the surface and help passivate the interfacial defects with the CTL. As a result, it reduces both the bulk and interfacial trap states to minimize the electron–hole recombination and helps transport photogenerated carriers to be collected by the electrodes smoothly. Most of the previous work has been based on a single halide passivation effect. Therefore, there is space for investigating the combined fluorine (F), chlorine (Cl), and bromine (Br) passivation effect in iodine (I)-based perovskites. The radius difference between I and Br is insignificant, so the diffused Br might share a bond in the perovskite octahedra. The radius difference between I and Cl is large, and the diffused Cl might engage in bond sharing in perovskite octahedra or might be a free atom. In the case of F, the radius difference between I and F is very large; therefore, the diffused F is probably a free or interstitial atom. At the same time, a three-dimensional/two-dimensional (3D/2D) bilayered perovskite could be formed, where the 2D perovskite works as a capping layer on top of the 3D perovskite thin film. The 2D capping layer works as a shield from the environmental surroundings and enhances the stability of the PSC.

Again, as an active layer, mixed halide perovskite offers flexibility to tune different optoelectronic properties.[6,7] Among different mixed halide perovskites, chloride–iodide is preferable to bromide–iodide.[8] Cl doping does not change the bandgap of iodide-based perovskite, while Br doping increases the bandgap and shifts toward the ultraviolet region. Cl doping in I-based perovskite exhibits attractive optoelectronic properties. The unchanged bandgap perfectly matches the mid-visible range, and the carrier lifetime increases with a diffusion length

---

[a] *School of Photovoltaic and Renewable Energy Engineering, UNSW Sydney, NSW, 2052, Australia. E-mail: a.howlader@unsw.edu.au, a.uddin@unsw.edu.au*
[b] *Mark Wainwright Analytical Centre, UNSW Sydney, NSW, 2052, Australia*

of more than 1 μm.[9] Along with these advantages, there are also challenges. One is their large radius mismatch.[8] Due to this reason, while mixing the Cl in I-based perovskite, the octahedron of the perovskite remains under local stress and strain. The local stress and strain create dangling bonds and free $Cl^-$ or $I^-$ ions. There is a possibility of self-formation of the $SnCl_2$ layer at the buried interface while depositing the chloride–iodide perovskite on top of the $SnO_2$ nanoparticle electron transport layer (ETL).[10] This unique phenomenon could occur due to the free halogen ions in the chloride–iodide-based perovskite. There is still a need for atomic-level inspection of this phenomenon. Therefore, atomic-level characterization studies are necessary to examine the buried interface closely.

Here, we chose bulky organic precursors named 4-fluorobenzylammonium chloride (4-FBAC) and 4-fluorobenzylammonium bromide (4-FBAB) to passivate the top surface of the chloride–iodide perovskite thin film. Fluorinated arylammonium halide has some advantages for use as an interfacial passivator. The electron-donating properties of F increase the electron density on the amine. Thus, the fluorinated bulky organic molecule offers a higher binding to acceptor-type defects on perovskite grain surfaces due to the highly electronegative F.[11,12] This property increases the probability of 2D perovskite formation kinetics. Thus, the fluorobenzylammonium-based 2D perovskite film offers a more homogeneous energy landscape and better carrier transport properties at the interface. This makes fluorobenzylammonium a perfect passivator for getting a higher fill factor. Besides playing a role in interfacial defect passivation, a fluorinated bulky organic molecule offers better hydrophobic properties.[13] The F at position four increases the lipophilic properties of the benzylammonium moiety. This enhances the hydrophobicity of the 2D perovskite film, which helps to get better stability against moisture of the PSC. Therefore, we get an improved 3D/2D bilayered PSC with a fluorinated benzylammonium moiety. We also achieve stability for a longer time.

This report proposes a PSC with a chloride–iodide perovskite ($FA_{0.6}MA_{0.4}PbI_{2.7}Cl_{0.3}$) deposited on a $SnO_2$ nanoparticle thin film. There is a self-formed $SnCl_2$ layer at the buried interface of $SnO_2$ and perovskite. The $SnCl_2$ layer is formed due to the $Sn^{2+}$ and $Cl^-$ ion migration in the $SnO_2$ and perovskite, respectively. We use high-resolution transmission electron microscopy (HRTEM) and high-resolution energy dispersive spectroscopy (HREDS) to closely observe the self-formed $SnCl_2$ layer at the buried interface of $SnO_2$ and perovskite. The free $I^-$ ions go to the opposite interface due to the repulsion by the $Cl^-$ ions. The bulk of the perovskite thin film lacks halogen ions. This imbalance can be mitigated by passivation of the top surface. Here, we combine two organic precursors (4-FBAC and 4-FBAB) to passivate the top surface of the chloride–iodide perovskite. We explore the effect of the combined diffusion of F, Cl, and Br in the chloride–iodide perovskite thin film with depth-dependent X-ray photoelectron spectroscopy (XPS) and time-of-flight secondary ion mass spectroscopy (ToF-SIMS). We optimize the different halogen concentrations to passivate the bulk defects in the perovskite thin film.[14] We also find that a 2D layer forms on the surface of the perovskite thin film. We observe a tremendous improvement in the fill factor (FF) and stability. Our champion PSC offers a photo conversion efficiency (PCE) of 21.10% with an open circuit voltage ($V_{oc}$) of 1.10 V, a short circuit current density ($J_{sc}$) of 25.15 mA $cm^{-2}$, and a FF of 76.44%. Our PSC also offers 80% of its initial PCE after 56 days of being kept under ambient conditions (temperature 25 °C, humidity 40%, and no illumination) without encapsulation. We obtained a 30% stability improvement in the passivated PSC compared to the non-passivated PSC.

## 2. Experimental methods

### 2.1 Required materials

The materials used in this experiment are listed as follows: tin(IV) oxide ($SnO_2$: 15% in $H_2O$ colloidal dispersion; Thermo Scientific), formamidinium iodide (FAI: 99.99%; Greatcell Solar Materials), methylammonium iodide (MAI: 99.99%; Greatcell Solar Materials), 4-fluorobenzylammonium chloride (99.99%; Greatcell Solar materials), 4-fluorobenzylammonium bromide (99.99%; Greatcell Solar materials), lead(II) iodide ($PbI_2$: 99.99%, trace metals basis; TCI), lead(II) chloride ($PbI_2$: 99.99%, trace metals basis; TCI), spiro-OMeTAD (Luminescence Technology), 4-*tert*-butylpyridine (*t*-BP: Sigma-Aldrich), bis(trifluoromethane) sulfonimide lithium salt (Li-TFSI: 99.95%, trace metals basis; Sigma-Aldrich), *N*,*N*-dimethylformamide (DMF: 99.8%, anhydrous; Sigma-Aldrich), dimethyl sulfoxide (DMSO: 99.9%, anhydrous; Sigma-Aldrich), chlorobenzene (99.8%, anhydrous; Sigma-Aldrich), acetonitrile (CAN: 99.8%, anhydrous; Sigma-Aldrich), isopropyl alcohol (99.9%, anhydrous; Sigma-Aldrich), and silver shot (4 N ESPI Metals).

### 2.2 Solution process

The 15% $SnO_2$ nanoparticle colloidal solution is diluted further to make a solution. This solution's $SnO_2:H_2O$ ratio is 1:1 (7.5% $SnO_2$). The solution is stirred for 1 hour. For the perovskite solution, FAI (51.6 mg), MAI (31.8 mg), $PbI_2$ (196 mg), and $PbCl_2$ (20.9 mg) are taken with these weights. The volumes of DMF and DMSO for the perovskite solutions are 400 μL and 100 μL, respectively. The solution is stirred for 6 hours. The spiro-OMeTAD solution is prepared with 36.15 mg in 500 μL of chlorobenzene. 14.4 μL 4-*tert*-butylpyridine and 8.7 μL Li-TFSI are mixed into that solution. The solution is stirred for 4 hours. The Li-TFSI solution is prepared with 52 mg in 100 μL of acetonitrile and stirred for 2 hours. The mixed organic precursor solution is prepared with 1.5 mg of 4-FBAC and 0.5 mg of 4-FBAB in 1 mL of isopropyl alcohol. The solutions are stirred for 4 hours.

### 2.3 Device fabrication

The patterned ITO (thickness 200 nm) glass substrates (1.2 cm × 1.2 cm) are cleaned with deionized water, acetone, ethanol, and 2-propanol for 10 minutes each. After that, the substrates are treated with $N_2$ gas flow and UV ozone gas for 1 and 20 minutes, respectively. The $SnO_2$ nanoparticle solution is spin-coated on the substrates outside the glovebox. The $SnO_2$

layer is spin-coated with two steps of the spinning condition: the first step with a spinning speed of 1000 rpm for 10 s and acceleration of 250 rpm; the second step with a spinning speed of 3000 rpm for 30 s and acceleration of 500 rpm. After that, the samples are annealed at 150 °C in open air for 20 minutes. Then, the samples are again treated with UV ozone gas for 10 minutes to oxidize the $SnO_2$ layer properly. The samples are then taken inside the glovebox. The perovskite solution is deposited on them under two-step spinning conditions. The first step is 1000 rpm spinning speed for 10 s with an acceleration of 250 rpm, and the second is 4000 rpm spinning speed for 40 s with an acceleration of 1000 rpm. The perovskite thin film (400 nm) is annealed at 110 °C for 10 minutes. Thus, the perovskite ($FA_{0.6}MA_{0.4}PbI_{2.7}Cl_{0.3}$) active layer is obtained. Then, the passivation layer (10 nm) is deposited in a two-step spin coating: 1000 rpm spinning for 10 s with an acceleration of 250 rpm and 5000 rpm spinning for 15 s with an acceleration of 500 rpm. Then it is annealed at 100 °C for 3 minutes. Then the spiro-OMeTAD layer (300 nm) is also deposited with a two-step spinning speed: the first step with a spinning speed of 1000 rpm for 10 s and acceleration of 250 rpm; the second step with a spinning speed of 3500 rpm for 35 s and acceleration of 500 rpm. Finally, the back electrode is deposited *via* thermal evaporation of Ag with a deposition rate of 2 Å $s^{-1}$, with a thickness of 100 nm, and the active area of the final device is 1 $cm^2$.

### 2.4 Device characterization

We use a NREL-calibrated Keithley 2400 Source Meter with 100 mW $cm^{-2}$ (AM 1.5G filter) simulated sunlight for our device's current–voltage characteristics measurement. EQE measurements are obtained using the QEX7 Spectral Response System. The absorption characterization is performed with a UV-vis-NIR spectrometer (PerkinElmer-Lambda 950). Using this spectrometer, we measure the transmittance ($T$) and reflectance ($R$) and calculate absorbance ($A$) from the relation $A = 1 - T - R$. Photoluminescence (PL) spectra and time-resolved photoluminescence (TRPL) are taken using a PL spectrometer and 532 nm LASER (EKSPLA, PT200; pulse width: 10 ps; frequency: 1 MHz). We carry out the impedance analysis on the Autolab PGSTAT-30 analyzer ($10^6$–$10^2$ Hz, 10 mV). The X-ray diffraction (XRD) is measured using a PANalytical Empyrean Thin-Film XRD machine with Cu Kα radiation, with a step size of 0.02°. We capture surface topology scanning electron microscopy (SEM) images and angle-resolved EDS analysis using a NanoSEM 230 fitted with a Bruker SDD-EDS detector. The sample holder is tilted at 30°, 45°, and 60°, and the sample surface creates a 60°, 45°, and 30° angle with the electron beam to take EDS from the very top portion of the surface. A Bruker Dimension ICON SPM is used to quantify the surface roughness with atomic force microscopy (AFM). Fourier transform infrared spectroscopy (FTIR) is performed using a PerkinElmer Spectrum 100 spectrometer fitted with attenuated total reflectance (ATR) and transmission accessories. We have carried out TOF-SIMS using a ION-TOF TOFSIMS 5 with a $Bi^+$ primary beam (30 keV and 0.45 pA) and a $Cs^+$ sputter beam (1 keV and 74.1 nA). XPS is carried out using an ESCALAB250Xi using a monochromatic Al Kα source (1486.68 eV, 120 W, 13.8 kV, 8.7 mA, $2 \times 10^{-9}$ bar), and depth profiling is carried out with an $Ar^-$ ion beam of 1 keV and a rate of 0.1 nm $s^{-1}$. Grazing incidence wide-angle X-ray scattering (GIWAXS) measurement is performed on a SmartLab (Rigaku) diffractometer equipped with a rotating anode X-ray tube and Cu Kα radiation source ($\lambda$ = 1.54 Å). The incident beam is conditioned using cross-beam optics to achieve a minute point focus of ∼400 μm, ensuring adequate spatial resolution. Data are collected at a fixed incident angle of 0.3° to probe near-surface structural information. 2D scattering patterns are acquired using a Hypix-3000 area detector (100 μm 2 pixel size) positioned 150 mm from the sample, in a single exposure of 300 s.

TEM helps us investigate the buried interface of perovskite/ETL at the atomic level. A couple of challenges are associated with the perovskite TEM analysis, and detailed discussions are rare in the literature. Here, we discuss all the procedures step-by-step. Before TEM analysis, preparing the perovskite sample with focused ion beam (FIB) milling is necessary to reduce its thickness to less than 100 nm. In the case of FIB, choosing every parameter carefully is essential; otherwise, the perovskite sample can be easily degraded. The sample is first attached to a SEM stub and then sputter-coated with a platinum (Pt) metal layer using the Leica ACE 600 coater. This is done for conductivity reasons and to protect the very top surface from the initial damage from the ion beam. The specimen is then loaded into the Thermo Fisher Helios G4 PFIB UXe Dual Beam system to prepare a thin cross-section lamella suitable for TEM. Once the region of interest is located and the eucentric height is set up, another thicker layer of platinum (∼1.5 μm) is deposited on top of the sample using an *in situ* Pt gas injection system (beam parameters are 12 kV with 300 pA beam current). Then, a trench is milled out using the plasma beam, so the small cross-section specimen could be removed using the *in situ* lift-out needle. The perovskite sample is sensitive to the heat generated by the plasma beam, and sample degradation can occur even in a vacuum under high beam energies. The beam conditions are reduced to the minimum practical level to mill the trench (voltage: 30 kV, beam current: 4 nA). Further decreasing the beam conditions is possible; however, the milling process will take too long, which becomes impractical. After extracting the sample using the *in situ* needle, it is welded to a copper half grid using platinum. The specimen is then slowly milled on both sides with progressively lower and lower beam conditions. Again, because of the beam-sensitive nature of the perovskite sample, the beam current is first reduced to 1 nA, and once the sample is thinned below 1 μm in thickness, the current is reduced to 0.3 nA. After the sample is thinned to below 500 nm, the beam current is reduced to 100 pA for further processing. Once the specimen is below 200 nm, the beam conditions are further reduced, and the voltage is set to 12 kV and the beam current to 30 pA. Finally, when the specimen thickness is below 100 nm, the specimen is further polished on both sides using an even gentler beam, the voltage is reduced to 5 kV, and the beam current is 10 pA. The milling process is stopped when the specimen is TEM transparent. TEM imaging is performed on cross-sectional samples using a Thermo Fisher Scientific Talos L120C microscope operating at an accelerating voltage of 120 keV and a beam current of 1 nA. High-angle annular dark field scanning transmission electron microscopy (HAADF-STEM segmented Panther) and HREDS element mapping are used to investigate the distribution of elemental species in the halide perovskite thin film. Images are captured using a Ceta-S camera and analysed using Velox Analytical Software (Thermo Fisher Scientific Electron Microscopy Solutions, Hillsboro, USA, TFS).

### 2.5 Device stability

We do the stability testing in ambient conditions (temperature range 25 °C to 30 °C, humidity range 40% to 50%). These are the conditions under which we take the *I–V* measurements each time. During the stability testing, we keep our PSCs in a desiccator chamber under controlled temperature and humidity (25 °C to 27 °C and 30% to 40% humidity range).

### 2.6 Simulation method

The geometry optimization of the chloride–iodide perovskite crystalline structure is done using the Vienna ab initio Simulation Package (VASP). The geometry optimization and electrostatic potential (ESP) map of BAC, 4-FBAC, BAB, and FBAB are simulated using the Avogadro software.

## 3. Results and discussion

The schematic diagram of our developed PSC is pictured in Fig. 1a. At the same time, in Fig. 1b, we sketch the electronic band diagram of the whole device. We choose chloride–iodide perovskite as the active layer. The ratio of the mixed halides in the perovskite is as follows: Cl (10%) and I (90%). We also use mixed organic cations in the perovskite with the ratio as follows: formamidinium (FA) (60%) and methylammonium (MA) (40%). Thus, the final chemical formula of the active perovskite layer becomes $FA_{0.6}MA_{0.4}PbI_{2.7}Cl_{0.3}$. This ratio of FA/MA is expected to improve moisture stability and provide a better crystalline structure.[15] It is also expected that this ratio of Cl/I should provide the best PCE, and for the ETL, we use 7.5% $SnO_2$ nanoparticle concentration for the best PCE expectation.[10] We use indium tin oxide (ITO) as the front electrode, 2,2′,7,7′-tetrakis-(*N*,*N*-di-4-methoxyphenylamino)-9,9′-spirobifluorene (spiro-OMeTAD) as the hole transport layer (HTL), and silver (Ag) as the back electrode. We also use mixed 4-FBAC and 4-FBAB as the top surface passivators. The chemical structure of these molecules is given in Fig. S1a and b. We simulate the electrostatic potential maps of BA and 4-FBA as represented in Fig. S2a and b. From those figures, we see that after F addition to the benzene ring, the negative potential increases in the amine, because the highly electronegative F has electron-donating ability.

Here, we deposit mixed 4-FBAC and 4-FBAB perovskite precursors on top of the perovskite thin film. The mixed passivators contain 100% F, Cl (0–100%), and Br (0–100%). This passivation allows us to explore the combined diffusion patterns of F, Cl, and Br. Before passivation, the perovskite has only I (90%) and Cl (10%). The Cl doping inside the I-populated matrix creates local stress or strain, especially in the octahedron. As a result, free $Cl^-$ and $I^-$ ions are created due to the dangling bonds. Due to the solution-processed fabrication, many atomic vacancies are present in the perovskite thin film and the $SnO_2$ nanoparticle ETL. The $SnO_2$ nanoparticle ETL also has atomic vacancies on its surface due to oxidation.[16] Sn, I, and Cl can move through these atomic vacancies. There are atomic vacancies in the bulk and surface of the $SnO_2$ nanoparticle ETL, and the Sn atoms diffuse towards the surface. After the deposition of a chloride–iodide perovskite thin film on top of the thin $SnO_2$ nanoparticle thin film, a unique phenomenon occurs. There is a game of coulombic attraction between $Sn^{2+}$ and $I^-$ or $Cl^-$ ions at this buried interface. As the electronegativity of Cl is more than I, here the coulombic attraction between the $Sn^{2+}$ and $Cl^-$ overcomes the coulombic attraction between the $Sn^{2+}$ and $I^-$. As a consequence, at least a monolayer of $SnCl_2$ might be formed at the buried interface.

Before exploring the combined diffusion behavior of F, Cl, and Br in the chloride–iodide perovskite thin film, we need to

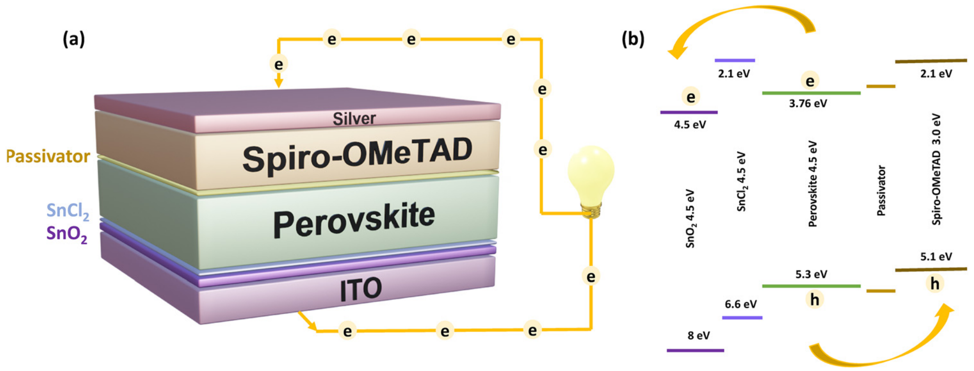

Fig. 1 (a) Schematic diagram of the passivated (mixed 4-FBAC and 4-FBAB) chloride–iodide PSC. (b) The electronic band diagram of the whole PSC without the front electrode (ITO) and back electrode (Ag). The mixed passivator forms a very thin two-dimensional layer, so the bandgap, valence band, and conduction band values are not mentioned for the layer.

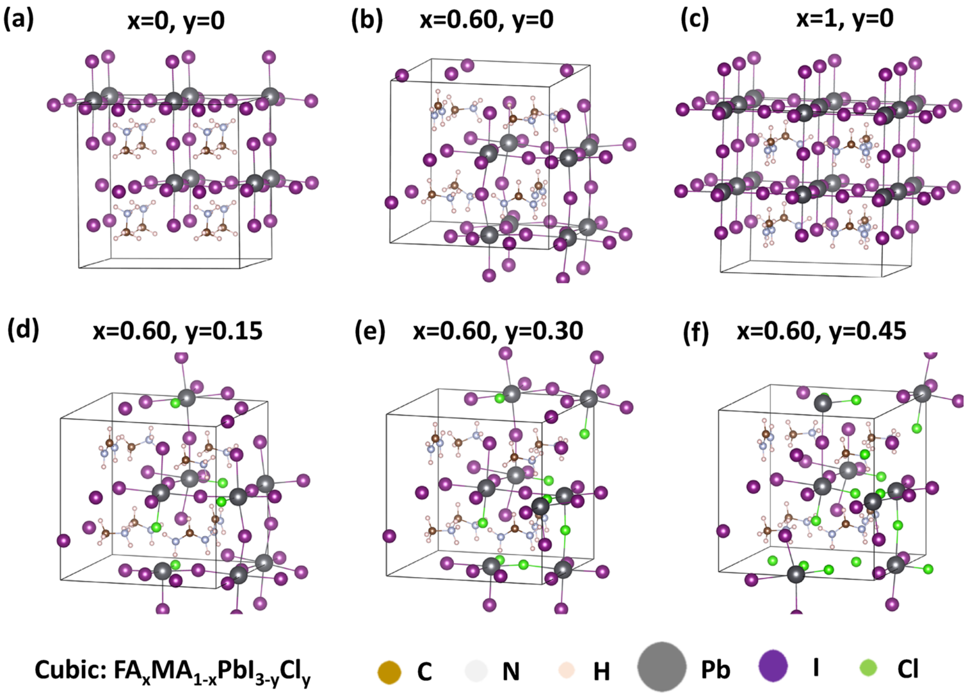

Fig. 2 Simulated cubic structures of (a) $MAPbI_3$, (b) $FA_{0.6}MA_{0.4}PbI_3$, (c) $FAPbI_3$, (d) $FA_{0.6}MA_{0.4}PbI_{2.85}Cl_{0.15}$, (e) $FA_{0.6}MA_{0.4}PbI_{2.70}Cl_{0.30}$, and (f) $FA_{0.6}MA_{0.4}PbI_{2.55}Cl_{0.45}$.

know the inside picture of the atomic arrangement of the iodide-perovskite with Cl doping. We simulate the atomic structure of our chloride–iodide perovskite with different concentrations of Cl doping. The cubic structures of $FA_xMA_{1-x}PbI_{3-y}Cl_y$ are shown in Fig. 2a–f with different $x$ and $y$ variations. Fig. 2a–c represent $MAPbI_3$, $FA_{0.6}MA_{0.4}PbI_3$, and $FAPbI_3$ respectively. We see perfect cubic structures with $MAPbI_3$ and $FAPbI_3$. We observe that the perovskite structure of $FA_{0.6}MA_{0.4}PbI_3$ is slightly deformed when FA and MA are present in a mixed proportion. From Fig. 2d–f, we see that the deformation of the $FA_{0.6}MA_{0.4}PbI_{3-y}Cl_y$ perovskite increases with increasing Cl concentration. Now we see the inside picture of the atomic arrangement of our chloride–iodide perovskite $FA_{0.6}MA_{0.4}Pb_{2.7}I_{0.3}$ (see Fig. 2e). Here, the regular atomic arrangement is deformed significantly inside the perovskite, especially the octahedron. The significant deformation occurs due to the mismatch of the atomic radii between Cl and I. Here, we expect the radius mismatch between Cl and I to produce local stress and strain. Therefore, there is a possibility of the creation of dangling bonds and free $Cl^-$ and $I^-$ ions.

Again, before exploring the combined diffusion behavior of F, Cl, and Br in the chloride–iodide perovskite thin film, we need to observe the buried interface of our PSC closely. Our PSC is of the n–i–p type and for this reason, most of the irradiance from the sun absorbs near the buried interface. Due to the higher number of photons absorbed near the buried interface, the recombination rate is also higher. In our PSC, the self-formed extremely thin $SnCl_2$ has deeper valence band compared to active perovskite layer, which helps to reduce the back recombination. We prepare a very thin cross-section of the perovskite film deposited on $SnO_2$/ITO/glass structure for this. After depositing Pt on top of the perovskite thin film, we prepare the cross-section with ion milling using a FIB. We take an HRTEM image of the cross-section as presented in Fig. 3a. The HRTEM image shows each Pt, perovskite, $SnO_2$ nanoparticles, ITO, and glass layer. We take HREDS from the cross-section. In Fig. 3b, a HADDF image of the cross-section is presented, which provides a clear view of each layer. Fig. 3c shows combined Sn, Cl, and I elemental mapping, and Fig. 3d–f show individual elemental mappings. Here, we observe the accumulation of Cl near the buried interface and the possible self-formation of $SnCl_2$. It is worth mentioning that we found the same energy signal from the Cl and Pt-rich area. This is probably due to the position of the characteristic Cl Kα and Pt Mα peaks in the close energy region of 2–3 keV.

We perform a detailed step-by-step analysis to explore the ion migration inside the bulk of the perovskite thin film after the passivation with mixed 4-FBAC and 4-FBAB. First, we perform depth-dependent energy-dispersive spectroscopy XPS. The results are taken from the nearby area of the perovskite/$SnO_2$ buried interface and are depicted in Fig. S3a. The movable ions on the perovskite side are $Pb^{2+}$, $F^-$, $Cl^-$, $Br^-$, and $I^-$, while $Sn^{2+}$ and $O^-$ are on the $SnO_2$ side. From the figure, we see that the atomic percentages of Pb, I, and O sharply decrease at the buried interface. The atomic percentages of F and Br are too low to count. On the other hand, the atomic percentage of Cl and Sn increases near the buried interface. Therefore, the probability of the self-formation of $SnCl_2$ is high at the buried interface. To verify this unique phenomenon, we also perform a depth-dependent TOF-SIMS from the buried interface as manifested in Fig. S3b. Here, we see the spatial concentration of all the different ions, especially near the

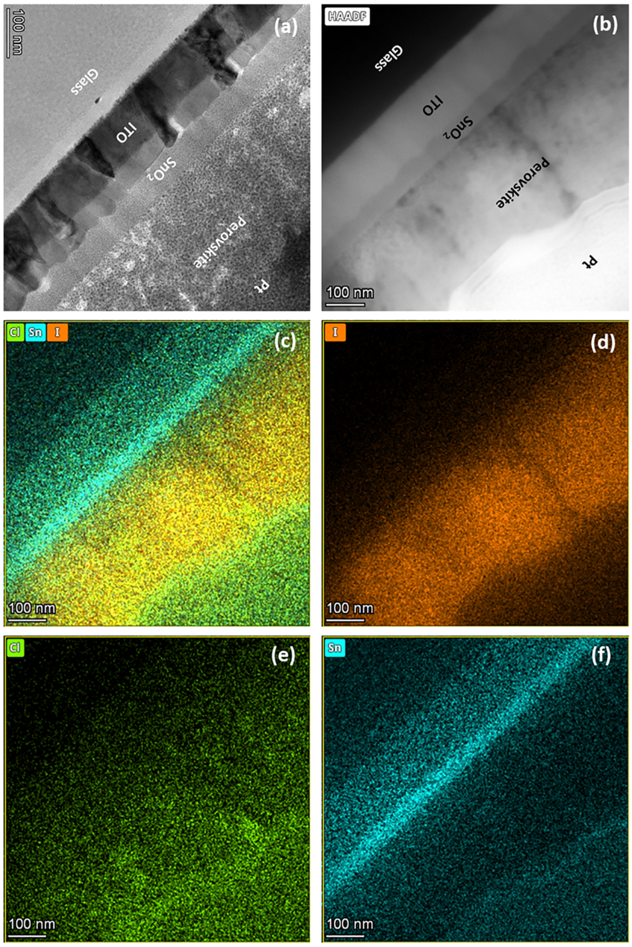

Fig. 3 (a) HRTEM cross-section image of the non-passivated chloride–iodide perovskite thin film. (b) HAADF image of the same cross-section. (c)–(f) HREDS mappings from the same area.

buried interface. The Pb, Br, I, and O counts sharply fall near the buried interface. In contrast, the counts of Cl, F, and Sn are higher at the buried interface. Therefore, there is a possibility of forming $SnCl_2$ and $SnF_2$. Between Cl and F, the Cl count is much higher than F because the concentration of Cl is higher than that of F in the perovskite matrix. These results support the self-formation of the $SnCl_2$ interface layer at the buried interface of chloride–iodide perovskite/$SnO_2$ ETL.[10]

We measure the quantity of halogens in the bulk of the chloride–iodide perovskite thin film. We investigate the F, Cl, Br, and I atom percentages from the bulk with depth-dependent EDS, which are tabulated in Table S1 (the corresponding EDSs are shown in Fig. S4a–d). The EDS detects the halogens from the surface towards the bulk. We see that the I concentration is much higher than the Cl in the bulk. We also notice that the quantity of the I remains constant and then decreases. The amount of Cl first increases and then decreases. On the other hand, F and Br are not the basic elements of the chloride–iodide perovskite; they come from the passivation. We see that the diffusion quantity of F reduces while the diffusion quantity of Br increases with depth. As the radius difference between I and Br is insignificant, Br could form bonds in the octahedron. On the other hand, the radius difference between I and F is quite large, so F becomes an interstitial atom. The F mainly aggregates near the top surface.

We also investigate the top surface of the perovskite thin film after passivation. We examine the surface of both samples (non-passivated and passivated) with XPS, from which we can observe the quantity of halogens on the surfaces of the two samples more closely. The measured percentages of atoms are given in Table S2. The table shows that the amount of C on the surface increases significantly, whereas both N and I reduce significantly. The rise in carbon (C) is due to bulky benzylammonium cations on the surface. The decrease of I is due to better dense crystallization with the passivation effect, and in the aftermath, fewer I atoms come out to the surface. Furthermore, we carry out an XPS analysis of C from the top surface of both non-passivated and passivated samples. The obtained results are illustrated in Fig. S5a and b. Table S3 tabulates the intensity values of different binding energies for different C 1s bonds. We see that both samples have three peaks at 288.60 eV, 286.60 eV, and 284.8 eV, representing the C=N/C=O bond, C–O/C–N/C–H bond, and C–C/C=C bond, respectively. The 288.60 eV and 286.60 eV peaks come from $FA^+$ or $MA^+$ cations where C=N, C–N, and C–H bonds are available. Again, as the samples are exposed to the air during XPS, these two peaks possibly occur due to the oxidation of the surface. Another peak representing the C–C/C=C bond comes from benzylammonium cations. The intensity of the related peak is higher in the benzylammonium passivated sample. This is the proof of the aggregation of bulky organic benzylammonium cations on the surface of the passivated sample. Another way to probe benzylammonium organic cations is to perform Fourier-transform infrared (FTIR) spectroscopy on the surfaces of both samples. After taking FTIR spectra on both samples, we observed that both samples showed peaks related to perovskite (see Fig. S6a).[17] We also observe some different peaks within the range from 800 to 1600 $cm^{-1}$ (see Fig. S6b) in the passivated sample. The extra peaks are 840, 1100, 1160, 1250, 1385, and 1520 $cm^{-1}$. Peaks within 1300–1600 $cm^{-1}$ come from C=C stretching, and those within 800–1300 $cm^{-1}$ come from C–H bending. The organic benzylammonium cation also possesses a C=C bond and a C–H bond, which belongs to the benzene ring.[18,19] Thus, FTIR results confirm the bulky organic benzylammonium cations on the surface plane of the passivated sample.

We analyze the crystalline properties of our two samples (non-passivated and passivated) using XRD. We find that the crystalline properties of the thin film improve after passivation. The passivated halogen atoms minimize the atomic vacancies and heal the dangling bonds. Halogen passivation helps achieve optimum bonding strength between halide atoms and their nearest neighboring atoms. As a result, the compactness of the polycrystalline thin film also improves. The XRD patterns of the two samples are presented in Fig. 4a, which shows the different crystalline features of the samples. We find a slight right shift of all the peaks in the passivated sample. This is an indication of the enhancement of compactness of the

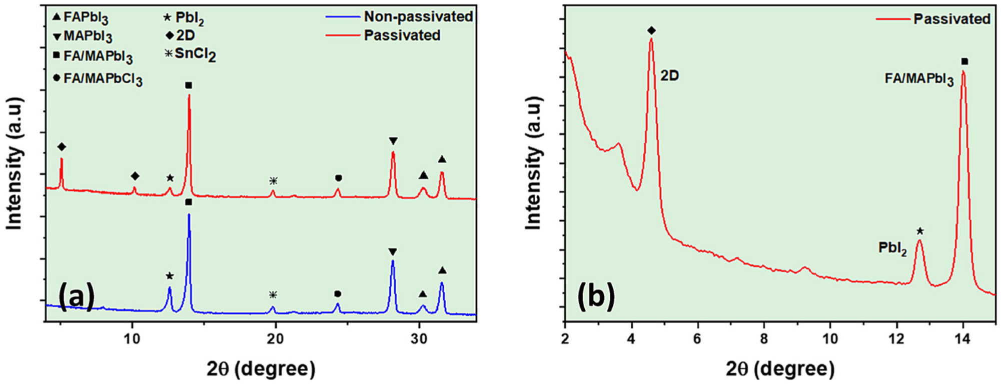

Fig. 4 (a) XRD analysis of both chloride–iodide perovskite samples (non-passivated and passivated). (b) GIWAXS of the passivated chloride–iodide perovskite sample.

crystalline structure after the passivation. We see a peak at 12.60° in both samples, corresponding to $PbI_2$, and significant suppression of its intensity in the passivated sample.[20] There is a large radius mismatch between Cl and I in the chloride–iodide-based perovskite. Due to local stress or strain, a structural deformation occurs in the perovskite, especially in the $PbI_6$ octahedral framework. Therefore, unbound ions like $Pb^{2+}$, $I^-$, and $Cl^-$ are created and move around the bulk of the perovskite thin film. The unbounded $I^-$ ions move toward the surface and react with $Pb^{2+}$ to form $PbI_2$. The benzylammonium bulky organic cation cannot diffuse into the bulk and stays on the surface of the perovskite thin film. There is a possibility of forming a 2D perovskite after interaction with the $PbI_2$ at the surface. We also see two peaks at 5.1° and 10.2° in the passivated perovskite sample, indicating 2D perovskite formation. We find a peak at 14°, which is related to both tetragonal $MAPbI_3$ and cubic $FAPbI_3$, and a peak at 28.15°, which is related to tetragonal $MAPbI_3$.[21,22] The peaks at 30.25° and 31.55° are related to the cubic $FAPbI_3$.[23] The peak at 24.35° is associated with the cubic $MAPbCl_3$/$FAPbCl_3$.[24,25] We do not find any peaks that are related to $SnO_2$[26] because the $SnO_2$ layer is nanocrystalline. We also do not find any peaks from ITO.[27] We see a peak around 19.80°, representing the characteristic peak of $SnCl_2$, and we do not see any peaks from $SnF_2$.[28] This is proof of the non-formation of $SnF_2$ at the buried interface, although F is more electronegative than Cl. We further analyze the crystalline properties of the passivated sample with GIWAXS to probe the 2D perovskite formation on top of the surface (see Fig. 4b). We find a strong peak at 4.60°, corresponding to the 2D perovskite.

We also took the morphological characteristics of the two samples using different microscopes. First, we use an atomic force microscope (AFM) to take surface images from the two chloride–iodide perovskite samples (non-passivated and passivated). We observe variations in the roughness of the surfaces before and after the passivation. We represent the 2D and 3D AFM images taken from the surfaces of the two different samples in Fig. 5a–d. We get mean roughness values from the two samples as 45.40 nm and 34.58 nm for non-passivated and passivated perovskite samples, respectively. The mean roughness value of the passivated sample reduces by about 10.82 nm after passivation. The bulky organic benzylammonium cations remain on the surface, and we get lower mean roughness. Due to the bulky shape, the organic benzylammonium cations are not able to penetrate the bulk of the perovskite thin film and stay on the surface. We also use a scanning electron microscope (SEM) to further analyze the morphological properties and take images from the surfaces as well as from the cross-section of the two perovskite samples, as shown in Fig. S7a–d. A visually clear morphological development is observed when the sample surface is treated with mixed 4-FBAC and 4-FBAB. Fig. S7a and c show that some grain boundaries are visible both on the surface and in the cross-section of the non-passivated chloride–iodide perovskite sample. In contrast, we see that the grain boundaries vanish both from the surface and cross-section (see Fig. S7b and d) after passivation. This is the proof of surface and bulk defect passivation by mixed 4-FBAC and 4-FBAB. The bulky organic cations help to reduce grain boundaries and voids.[29] Besides passivating the surface defects by bulky organic cations, halide ion diffusion also passivates bulk defects like atomic vacancies and grain boundaries.[30]

We vary the Cl and Br passivation ratio to sort out the optimum passivation and find the optimum passivation condition as 75% Cl and 25% Br. The PCEs of the non-passivated control and passivated champion cells are presented in Fig. 6a. We get an about 2.20% improvement in PCE after passivation from the champion cell. We obtain a PCE of 21.10% from the passivated champion cell and 18.90% from the non-passivated control cell. The open circuit voltage ($V_{oc}$) improves by about 3% in the passivated champion cell from the non-passivated control cell. We obtain the $V_{oc}$ of 1.10 V from the passivated champion cell, whereas 1.07 V from the non-passivated control cell. The short circuit current density ($J_{sc}$) improves by about 1.70% in the passivated champion cell compared to the non-passivated control cell. We obtain the $J_{sc}$ of 25.15 mA cm$^{-2}$ from the passivated champion cell, whereas 24.73 mA cm$^{-2}$ from the non-passivated control cell. We also get tremendous improvement in the fill factor (FF). The FF improves by about 5% in the passivated champion cell compared to the non-

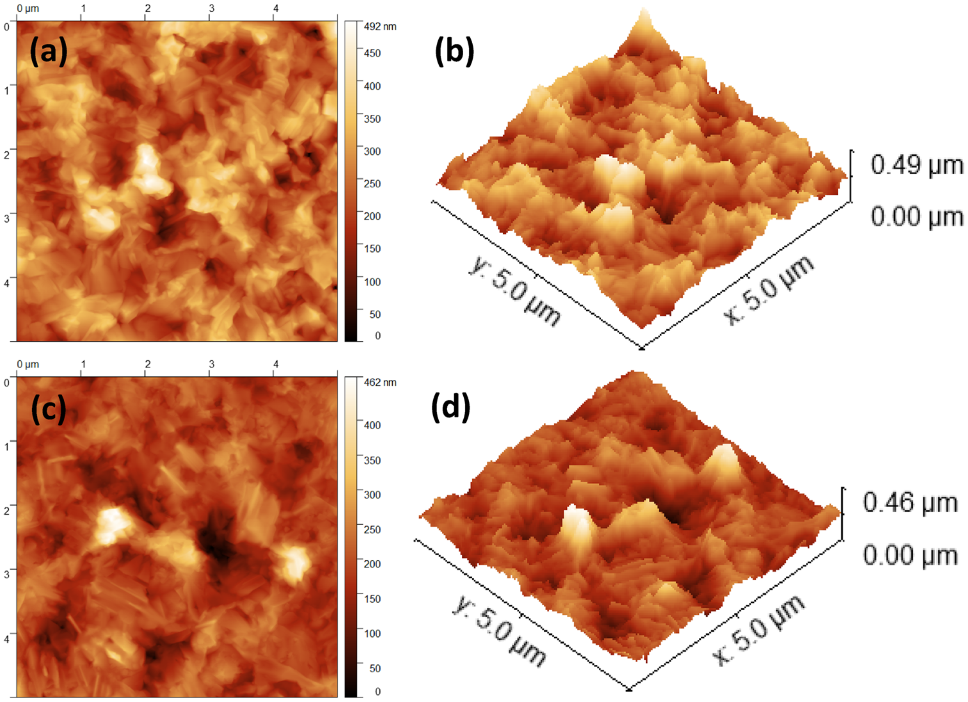

Fig. 5 2D AFM images of (a) non-passivated and (c) passivated chloride–iodide perovskite samples. 3D AFM images of (b) non-passivated and (d) passivated chloride–iodide perovskite samples. The AFM images are taken from the top surface of those chloride–iodide perovskite samples.

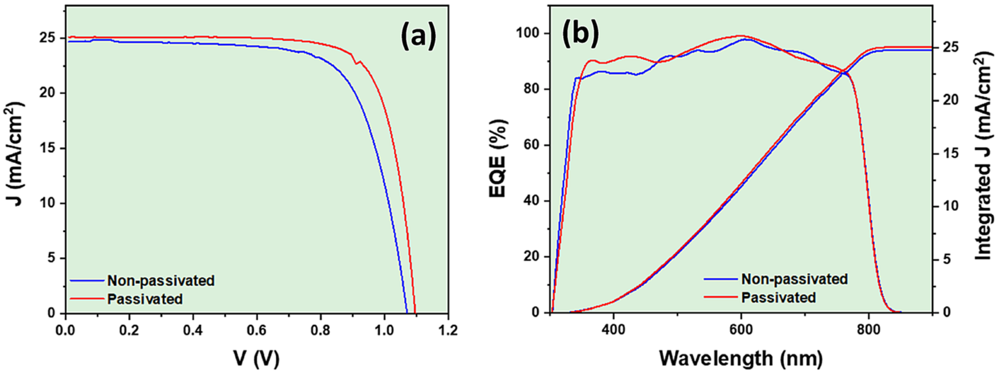

Fig. 6 Comparison of (a) PCE and (b) EQE with cumulative current density between the non-passivated control and passivated champion chloride–iodide PSC.

passivated control cell. We obtain an FF of 76.44% from the passivated champion cell, whereas 71.28% is from the non-passivated control cell. The statistical distribution of each key photovoltaic parameter of $V_{oc}$, $J_{sc}$, FF, and PCE for each cell type (6 cells for each type) is demonstrated in Fig. S8a–d. At the same time, Table S4 lists the average with standard deviation values and the champion values of each key photovoltaic parameter. Besides the self-formed $SnCl_2$ layer, the organic halide passivator plays the main role in improving efficiency.[31] The bulky organic cations and the halide ions passivate the surface as well as the bulk defects. The combined F, Cl, and Br passivation works as a tonic to improve the thin film morphology, crystallinity, and FF.

Due to internal ion migration, hysteresis is a common phenomenon in the *J*–*V* characteristic curve in PSCs.[32] The forward and reverse sweep *J*–*V* curves of the two PSCs (non-passivated and passivated champion cells) are presented in Fig. S9a and b. In most cases, the PCE in the forward sweep shows better PCE than in the reverse sweep. In the literature, the hysteresis index is calculated using different equations.[33,34] Among them, we calculate the hysteresis index using the formula that Severin *et al.* gave.[34] The calculated hysteresis index of the two PSCs is as follows: non-passivated control cell – hysteresis index is 1.5%, and passivated champion cell – hysteresis index is 0.60%. We see that the hysteresis index of the passivated PSC is 0.90% less than that of the non-passivated

PSC. This implies that the ion migration is reduced in the passivated PSC and indicates the perfect bulk passivation in the perovskite thin film.

In Fig. 6b, the external quantum efficiency (EQE) of the two PSCs (non-passivated control and passivated champion cells) is illustrated. The passivated champion PSC offers a higher response, especially in the smaller wavelength range. Consequently, the cumulative $J_{sc}$ of the passivated champion PSC surpasses the non-passivated one. The cut-off wavelengths from the EQE results of the two PSCs are presented in Fig. S10a. There is no significant difference in the cut-off wavelengths of the PSCs. We also take the absorption spectrum of the two samples. The absorption characteristics of the two samples are manifested in Fig. 7a. As expected, the absorption quantity increases for the whole wavelength range in the case of the passivated sample. The corresponding Tauc plot from the absorption data is presented in Fig. S10b. Unlike the cut-off wavelengths from EQE measurements, we find that the bandgap reduces after passivation. The bandgap reduces from 1.54 eV to 1.53 eV in the sample passivated with mixed 4-FBAC and 4-FBAB. Tan *et al.*[35] found that shallow interstitial defects can be generated unintentionally during post-fabrication treatments of the perovskite thin film surface with iodide organic perovskite precursors. In our case, the possible reason is that there might be interstitial $F^-$ ions as we find that they aggregate near the top surface. As the $F^-$ ions are the largest halide ions here, they become interstitial ions. The interstitial $F^-$ ions are the reason for the shallow energy states and the band gap reduction. Zhu *et al.*[36] also find that, ultra-shallow near-edge states improve carrier properties that enhance device performance.

The photoluminescence (PL) spectra of the two samples (non-passivated control and passivated champion) are illustrated in Fig. 7b. Here, the PL peaks follow a similar trend to the absorption data. Similar to the absorption spectra, the intensity of the PL peak increases after passivation. The time-dependent photoluminescence (TRPL) spectra of the two samples are shown in Fig. 7c. The TRPL curves are fitted with time constants $t_1$ and $t_2$ in an exponential second-order decay equation. We tabulated the time constants in Table S5. A higher $t_1$ value suggests a low trap state density in the bulk.[37] In our case, the low trap state density should be achieved only when the halogen defects in the bulk are passivated with likely halogens. Table S5 shows that the $t_1$ value for the passivated champion sample is about 1.5 times higher than for the non-passivated control sample. Therefore, we can claim the optimum halogen passivation in the bulk.

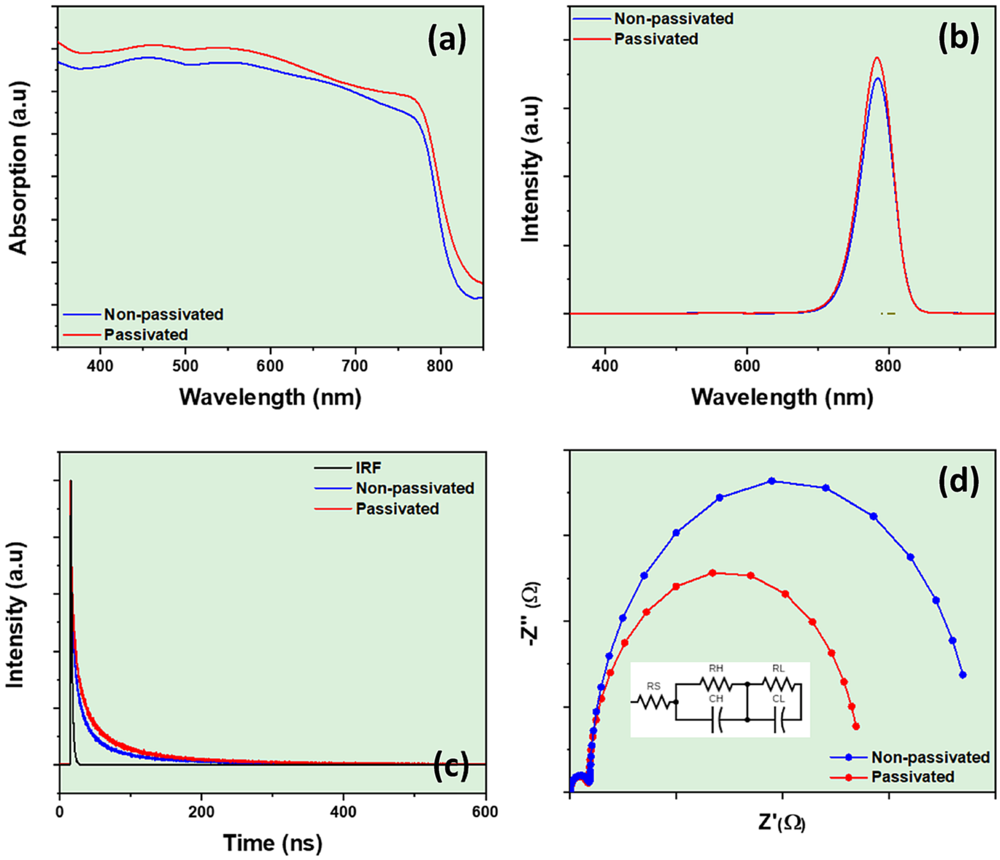

Fig. 7 Comparison of different optoelectrical properties between the two samples (non-passivated control and passivated champion): (a) absorption spectra, (b) PL spectra, and (c) TRPL. (d) Comparison of electrochemical properties with EIS between the two PSCs (non-passivated control and passivated champion cells).

Electrochemical impedance spectroscopy (EIS) explains more about ion migration and hysteresis of PSC.[38] Two distinct regions of frequency behaviors are obtained from the PSCs in EIS. Ion transport occurs with low frequency, and electron transport occurs with high-frequency bias voltage (here we use 1 mV bias voltage). We experiment with dark conditions because photo-generated electrons make the situation more complex. There are two loops in the EIS of our samples, as shown in Fig. 7d. In the higher frequency region, we see a smaller loop related to the electron transport. In the lower frequency region, we see a larger loop related to the ion transport. The real axis stands for the resistance, and the imaginary axis stands for capacitive reactance. The resistance (high-frequency $R_H$ and low-frequency $R_L$) and capacitance (high-frequency $C_H$ and low-frequency $C_L$) values are summarised in Table S6. If we analyze the results, we see that the capacitive values increase a little bit while the resistive value decreases significantly. $R_s$ and $R_H$ are lower for the passivated PSC, while the $R_L$ value decreases drastically. Fewer free ions cause fewer collisions and lower resistance for ions. That means the passivated PSC possesses fewer free ions, most of which are in bond formation with other atoms, which indicates bulk and interfacial defect passivation.

The optimum bulk passivation should reduce the trap state density of the PSC. To verify this, we calculate the trap density states of the two PSCs. We measure the current density *vs.* voltage values in dark conditions (see Fig. 8a). Here we see two different regions: the ohmic and the trap-filled limit regions. The trap density of states depends on the trap-filled limit voltage, which lies between the ohmic and trap-filled limit region. We determine the trap density states according to Richard *et al.*[39] The trap density of states ($n_{\text{trap}}$) is calculated using the following relation: $n_{\text{trap}} = (V_{\text{TFL}} \times 2\varepsilon_0\varepsilon)/(e \times d^2)$, where $V_{\text{TFL}}$ is the trap-filled limited voltage (the vertical dotted lines in Fig. 8a) ($V_{\text{TFL}}$ for non-passivated control cell = 0.9 V, $V_{\text{TFL}}$ for passivated champion cell = 0.75 V), $d$ is the thickness between the front and back electrode (its value is 1 μm (ITO = 200 nm, perovskite = 400 nm, spiro-OMeTAD = 300 nm, and Ag = 100 nm) approximately), $\varepsilon$ is the relative permittivity for $MAPbI_xCl_{1-x}$ and its value is 20,[40] $\varepsilon_0$ is the constant of permittivity in free space ($8.854 \times 10^{-14}$ F cm$^{-1}$), and $e$ is the coulombic charge of the electron ($1.61 \times 10^{-19}$ C). At the end of the calculation, we find the number of trap density states: $1.99 \times 10^{15}$ cm$^{-3}$ (non-passivated PSC) and $1.66 \times 10^{15}$ cm$^{-3}$ (passivated PSC). The trap density decreases at about $0.33 \times 10^{15}$ cm$^{-3}$, which is an improvement.

Fig. 8b represents the stability comparison of the two PSCs (non-passivated control and passivated champion cells). For the stability measurement, we do not use any encapsulation on the PSCs and test the PSCs in ambient conditions (temperature 25 °C to 30 °C, humidity range 40% to 50%). The PCE of the non-passivated control cell preserves about 80% and the passivated champion cell preserves about 80% of their initial efficiencies after 56 days. The possible reason lies in bulky organic benzylammonium cations at the interface of perovskite/HTL, which protect against moisture. A potential factor might be the formation of 2D perovskite on a 3D perovskite surface due to the bulky organic cations, which act as a capping layer.[41] The bulky organic benzylammonium cations passivate the surface while reducing the interfacial defects with HTL. The lowered interfacial defects also upgrade the stability against moisture because these interfacial defects are the Achilles' heel in the PSC, and water or oxygen molecules can easily diffuse through the perovskite film. The 3D perovskite-based PSC shows low stability, whereas the 2D perovskite-based PSC exhibits good immunity to environmental elements like light, heat, and moisture.[42,43] Again, after 56 days, as the humidity is near 40% to 50%, just like ambient air at room temperature, the non-passivated perovskite control sample turns yellow, which is due to the decomposition of the 3D perovskite structure, leaving yellow $PbI_2$. On the other hand, the passivated perovskite champion sample remains black without decomposition. Another possible reason for getting better stability might be the $Br^-$ ion doping in the chloride–iodide PSC. A small amount of

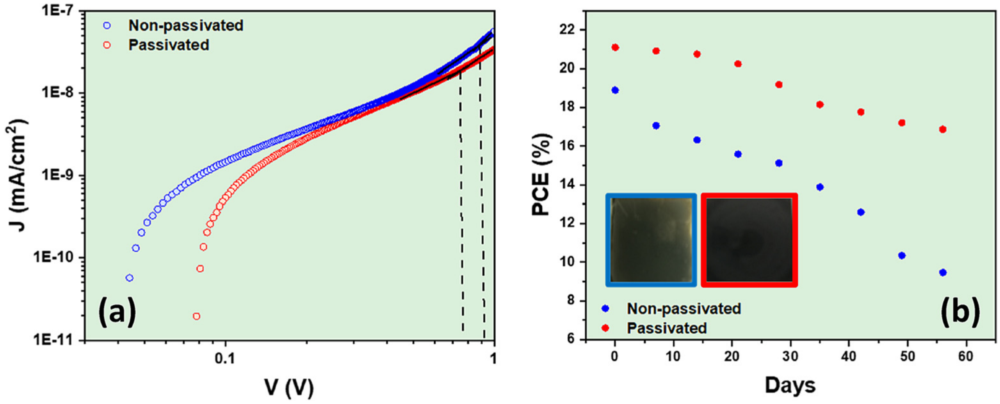

Fig. 8 Comparison between passivated champion and non-passivated control chloride–iodide PSCs: (a) trap density states and (b) stability without encapsulation. The inset shows the perovskite film (the blue-colored border is a non-passivated control perovskite film, and the red-colored border is a passivated champion perovskite film) after 56 days. After 56 days, we see that the non-passivated control sample becomes slightly yellowish, while the passivated champion sample remains black.

$Br^-$ ion doping helps to resist the perovskite (especially those perovskites containing FA cations) transforming into a yellow phase (the unstable perovskite phase) from a black phase (the stable perovskite phase).[44,45] At the same time, the formation of the 2D layer also depends on the proper choice of the passivating precursor's halide component. It is observed that among different halide components, Cl or Br-containing ones are most effective in forming a 2D capping layer on top of the 3D perovskite layer.[46]

## 4. Conclusions

Next-generation solar cells are achieving higher PCE values, especially with halide perovskite. Halogen doping is an effective way to manipulate the optoelectronic properties of halide perovskite. Between Br and Cl, Cl is preferable for doping in popular I-based perovskite. Cl doping helps to keep the bandgap within a suitable mid-visible range for solar energy harvesting. At the same time, it enhances the charge carrier's diffusion length significantly. Besides, due to the solution processability of perovskite thin film, there is a massive opportunity for large-scale roll-to-roll production of PSCs cheaply. The presence of atomic vacancies in the bulk of the solution-processed perovskite thin film needs special treatment. Although perovskite is quite defect-resistant, defects like atomic vacancies create many challenges, such as hysteresis and charge-trapping. Ion migration is a well-known phenomenon in perovskite, and it is mainly believed that atomic vacancies are the possible source of ion migration. The hysteresis and charge-trapping degrade the PCE ultimately. In the case of chloride–iodide perovskite, there is a large radius mismatch between Cl and I atoms. After the Cl doping, local stress or strain occurs, especially in the octahedron. Thus, dangling bonds are created, and more Cl or I atoms can move around the perovskite matrix. In our PSC, we deposit the chloride–iodide perovskite ($FA_{0.6}MA_{0.4}PbI_{2.7}Cl_{0.3}$) thin film on the $SnO_2$ nanoparticle thin film, the ETL. Due to the solution process, there are many atomic vacancies in the bulk of the ETL. Again, there are also many atomic vacancies on the surface of the ETL due to oxidation. Here in the ETL, the $Sn^{2+}$ ions diffuse to the buried interface of the ETL/perovskite through the atomic vacancies. On the perovskite side, the free $Cl^-$ and $I^-$ ions also try to move toward the buried interface. In this race between $I^-$ and $Cl^-$ ions, as the $Cl^-$ ion is more electronegative than the $I^-$ ion, the $Cl^-$ ion overcomes the $I^-$ ion, and the coulombic attraction between $Sn^{2+}$ and $Cl^-$ ions wins. There is a probability of a new unique phenomenon of self-formation of the $SnCl_2$ interface layer. Due to this phenomenon, there is a scarcity of halide ions in the bulk of the perovskite thin film. So, we need to do halide passivation from the top surface of the perovskite. Here, we use mixed 4-FBAC and 4-FBAB as the passivators on the top surface. The bulky organic benzylammonium cations remain on the surface and help to passivate the interfacial defects with the hole transport layer. The halide ions diffuse through the bulk of the thin film and mitigate the bulk defects. We obtained 21.10% PCE in our passivated champion cell. Also, the stability of the cell is about 80% after 56 days without encapsulation. This device allows us to explore the combined F, Cl, and Br diffusion effects in the bulk of the perovskite thin film. We go through a detailed analysis to explore the diffusion pattern from the top surface of the perovskite thin film toward the buried interface.

## Author contributions

Author contributions are given below: A. H. H.—original draft; A. U.—manuscript correction; A. H. H.—design of experiments; A. H. H.—PSC fabrication and *J–V* curves; A. H. H.—PSC aging and operation test, A. H. H., Y. Y., R. K.—PSC characterization, data acquisition and validation; and A. U.—funding acquisition and supervision.

## Conflicts of interest

The authors declare no conflict of interest. All authors agreed to the current version of the manuscript.

## Data availability

All relevant data are within the manuscript and its supplementary information (SI). Supplementary information is available. See DOI: **https://doi.org/10.1039/d5ya00164a**.

## References

1 S. S. Kahandal, R. S. Tupke, D. S. Bobade, H. Kim, G. Piao, B. R. Sankapal, Z. Said, B. P. Pagar, A. C. Pawar, J. M. Kim and R. N. Bulakhe, *Prog. Solid State Chem.*, 2024, **74**, 100463.
2 M. J. M. Marques, W. Lin, T. Taima, S. Umezu and Md Shahiduzzaman, *Mater. Today*, 2024, **78**, 112–141.
3 Z. Guo, M. Yuan, G. Chen, F. Liu, R. Lu and W.-J. Yin, *Adv. Sci.*, 2024, **11**, 2305799.
4 Z. Wang, H. Gao, D. Wu, J. Meng, J. Deng and M. Cui, *Molecules*, 2024, **29**, 2104.
5 D. Li, Z. Xing, X. Meng, X. Hu, T. Hu and Y. Chen, *CCS Chem.*, 2023, **5**, 781–801.
6 L. Chouhan, S. Ghimire, C. Subrahmanyam, T. Miyasaka and V. Biju, *Chem. Soc. Rev.*, 2020, **49**, 2869–2885.
7 F. J. Iftikhar, Q. Wali, S. Yang, Y. Iqbal, R. Jose, S. Munir, I. A. Gondal and M. E. Khan, *Org. Electron.*, 2021, **91**, 106077.
8 A. H. Howlader and A. Uddin, *Nanomanufacturing*, 2023, **3**, 177–216.
9 S. D. Stranks, G. E. Eperon, G. Grancini, C. Menelaou, M. J. P. Alcocer, T. Leijtens, L. M. Herz, A. Petrozza and H. J. Snaith, *Science*, 2013, **342**, 341–344.
10 A. H. Howlader, S. S. Dipta, W. B. Tarique, Y. Qi, A. Pratik, Y. Yin, M. A. Hossain and A. Uddin, *Adv. Energy Sustainability Res.*, 2024, 2400030.
11 R. Lin, J. Xu, M. Wei, Y. Wang, Z. Qin, Z. Liu, J. Wu, K. Xiao, B. Chen, S. M. Park, G. Chen, H. R. Atapattu, K. R. Graham,

J. Xu, J. Zhu, L. Li, C. Zhang, E. H. Sargent and H. Tan, *Nature*, 2022, **603**, 73–78.

12 Y. Wang, R. Lin, C. Liu, X. Wang, C. Chosy, Y. Haruta, A. D. Bui, M. Li, H. Sun, X. Zheng, H. Luo, P. Wu, H. Gao, W. Sun, Y. Nie, H. Zhu, K. Zhou, H. T. Nguyen, X. Luo, L. Li, C. Xiao, M. I. Saidaminov, S. D. Stranks, L. Zhang and H. Tan, *Nature*, 2024, **635**, 867–873.

13 M.-G. La-Placa, L. Gil-Escrig, D. Guo, F. Palazon, T. J. Savenije, M. Sessolo and H. J. Bolink, *ACS Energy Lett.*, 2019, **4**, 2893–2901.

14 A. Hossain Howlader, W. Binte Tarique, S. Safat Dipta, A. Pratik, Y. Yin and A. Uddin, *Sol. Energy*, 2024, **282**, 112968.

15 Z. Liu, P. Liu, M. Li, T. He, T. Liu, L. Yu and M. Yuan, *Adv. Energy Mater.*, 2022, **12**, 2200111.

16 Z. Wang, R. Lin, Y. Huo, H. Li and L. Wang, *Adv. Funct. Mater.*, 2022, **32**, 2109503.

17 D. Yerezhep, Z. Omarova, A. Aldiyarov, A. Shinbayeva and N. Tokmoldin, *Molecules*, 2023, **28**, 1288.

18 S. Albert, K. Keppler, P. Lerch, M. Quack and A. Wokaun, *J. Mol. Spectrosc.*, 2015, **315**, 92–101.

19 C. Zhou, Z. Chen, G. Zhang, C. McDowell, P. Luo, X. Jia, M. J. Ford, M. Wang, G. C. Bazan, F. Huang and Y. Cao, *Adv. Energy Mater.*, 2018, **8**, 1701668.

20 C. Wu, K. Chen, D. Y. Guo, S. L. Wang and P. G. Li, *RSC Adv.*, 2018, **8**, 2900–2905.

21 P. Basumatary and P. Agarwal, *J. Mater. Sci.: Mater. Electron.*, 2020, **31**, 10047–10054.

22 S. M. Jassim, N. A. Bakr and F. I. Mustafa, *J. Mater. Sci.: Mater. Electron.*, 2020, **31**, 16199–16207.

23 Y. Zhou, M. Yang, J. Kwun, O. S. Game, Y. Zhao, S. Pang, N. P. Padture and K. Zhu, *Nanoscale*, 2016, **8**, 6265–6270.

24 X. Cheng, L. Jing, Y. Zhao, S. Du, J. Ding and T. Zhou, *J. Mater. Chem. C*, 2018, **6**, 1579–1586.

25 A. El-Yahyaoui, B. Jaber, L. Laanab, M. El Mahi and E. M. Lotfi, *J. Mater. Sci.: Mater. Electron.*, 2023, **34**, 252.

26 G. E. Patil, D. D. Kajale, V. B. Gaikwad and G. H. Jain, *Int. Nano Lett.*, 2012, **2**, 17.

27 Z. Ghorannevis, E. Akbarnejad and M. Ghoranneviss, *J. Theor. Appl. Phys.*, 2015, **9**, 285–290.

28 J. Tan, T. Lu, J. Zhang, B. Xie, M. Chen and X. Zhu, *J. Taiwan Inst. Chem. Eng.*, 2018, **86**, 18–24.

29 C. Fei, M. Zhou, J. Ogle, D.-M. Smilgies, L. Whittaker-Brooks and H. Wang, *J. Mater. Chem. A*, 2019, **7**, 23739–23746.

30 E. A. Alharbi, A. Y. Alyamani, D. J. Kubicki, A. R. Uhl, B. J. Walder, A. Q. Alanazi, J. Luo, A. Burgos-Caminal, A. Albadri, H. Albrithen, M. H. Alotaibi, J.-E. Moser, S. M. Zakeeruddin, F. Giordano, L. Emsley and M. Grätzel, *Nat. Commun.*, 2019, **10**, 3008.

31 V. Larini, M. Degani, G. Pica, C. Ding, Z. Andaji-Garmaroudi, F. Faini, S. D. Stranks, C.-Q. Ma and G. Grancini, *Sol. RRL*, 2022, **6**, 2200038.

32 N. K. Elumalai and A. Uddin, *Sol. Energy Mater. Sol. Cells*, 2016, **157**, 476–509.

33 Y. Rong, Y. Hu, S. Ravishankar, H. Liu, X. Hou, Y. Sheng, A. Mei, Q. Wang, D. Li, M. Xu, J. Bisquert and H. Han, *Energy Environ. Sci.*, 2017, **10**, 2383–2391.

34 S. N. Habisreutinger, N. K. Noel and H. J. Snaith, Hysteresis Index: A Figure without Merit for Quantifying Hysteresis in Perovskite Solar Cells, *ACS Energy Lett.*, 2018, **10**, 2472–2476.

35 S. Tan, I. Yavuz, M. H. Weber, T. Huang, C.-H. Chen, R. Wang, H.-C. Wang, J. H. Ko, S. Nuryyeva, J. Xue, Y. Zhao, K.-H. Wei, J.-W. Lee and Y. Yang, *Joule*, 2020, **4**, 2426–2442.

36 X. Zhu, W. Xiong, C. Hu, K. Mo, M. Yang, Y. Li, R. Li, C. Shen, Y. Liu, X. Liu, S. Wang, Q. Lin, S. Yuan, Z. Liu and Z. Wang, *Adv. Mater.*, 2024, **36**, 2309487.

37 E. V. Péan, S. Dimitrov, C. S. D. Castro and M. L. Davies, *Phys. Chem. Chem. Phys.*, 2020, **22**, 28345–28358.

38 D. A. Jacobs, H. Shen, F. Pfeffer, J. Peng, T. P. White, F. J. Beck and K. R. Catchpole, *J. Appl. Phys.*, 2018, **124**, 225702.

39 R. H. Bube, *J. Appl. Phys.*, 1962, **33**, 1733–1737.

40 M. Samiee, S. Konduri, B. Ganapathy, R. Kottokkaran, H. A. Abbas, A. Kitahara, P. Joshi, L. Zhang, M. Noack and V. Dalal, *Appl. Phys. Lett.*, 2014, **105**, 153502.

41 T. M. Koh, V. Shanmugam, X. Guo, S. S. Lim, O. Filonik, E. M. Herzig, P. Müller-Buschbaum, V. Swamy, S. T. Chien, S. G. Mhaisalkar and N. Mathews, *J. Mater. Chem. A*, 2018, **6**, 2122–2128.

42 D. H. Cao, C. C. Stoumpos, O. K. Farha, J. T. Hupp and M. G. Kanatzidis, *J. Am. Chem. Soc.*, 2015, **137**, 7843–7850.

43 I. C. Smith, E. T. Hoke, D. Solis-Ibarra, M. D. McGehee and H. I. Karunadasa, *Angew. Chem., Int. Ed.*, 2014, **53**, 11232–11235.

44 M. Pratheek, P. Sujith, T. A. Shahul Hameed and P. Predeep, *Mater. Lett.*, 2022, **326**, 132903.

45 F. Han, W. Yang, H. Li and L. Zhu, *Nanoscale Res. Lett.*, 2020, **15**, 194.

46 X. Liu, T. Webb, L. Dai, K. Ji, J. A. Smith, R. C. Kilbride, M. Yavari, J. Bi, A. Ren, Y. Huang, Z. Wang, Y. Shen, G. Shao, S. J. Sweeney, S. Hinder, H. Li, D. G. Lidzey, S. D. Stranks, N. C. Greenham, S. R. P. Silva and W. Zhang, *Energy Environ. Mater.*, 2022, **5**, 670–682.